Fixed-Frequency Parity-Time Symmetric Operation Using a Dual-Side Active Tuning Method for Wireless Power Transfer Systems

Ruozhong Gao, Xin Dai, *Member, IEEE*, Shijun Zhao, *Member, IEEE*, Pengqi Deng, Jinde Wu, and Yanling Li

***Abstract*—In conventional parity-time (PT)-symmetric wireless power transfer systems, capacitance drift, an unavoidable factor in practical applications, can induce detuning between the transmitter (Tx) and receiver (Rx), thereby degrading system performance. In addition, significant frequency variations arising from the frequency-dependent nonlinear saturation gain can lead to regulatory noncompliance and complicate filter design. This article proposes a simple dual-side active tuning method to achieve fixed-frequency PT-symmetric operation. Synchronous series compensators are introduced to ensure balanced energy distribution between the Tx and Rx. Active matching adjustment is required only on the Rx-side compensator, whereas the Tx-side compensator self-adjusts automatically. Theoretical analysis indicates that both the output voltage and transfer efficiency remain robust against variations in compensation capacitance, self-inductance, coupling coefficient, and load. Moreover, a parallel inductor at the inverter output achieves zero-voltage switching across the entire operating range. Experimental results demonstrate that the system maintains a constant output voltage across a wide coupling coefficient range (0.109–0.518), even with over 14% variation in compensation capacitance and 10.68% variation in self-inductance.**

***Index Terms*—Dual-side active tuning, fixed frequency, parity-time (PT) symmetry, synchronous series compensator (SSC), wireless power transfer (WPT).**

I. Introduction

WIRELESS power transfer (WPT) enables power transmission without the need for physical cables, offering significant advantages in flexibility, reliability, and safety. However, achieving robust power delivery and efficieny under varying coupling conditions remains a fundamental challenge in WPT systems. In recent years, parity-time (PT) symmetry has emerged as an effective solution to address this issue. PT symmetry, a concept originally from quantum physics, was first applied to WPT systems by Assawaworrarit et al. [1], where the transfer power and efficiency remain constant within a certain range of the coupling coefficient. According to PT-symmetry theory, a system is considered PT symmetric if it is invariant under parity inversion (P), time inversion (T). In such a system, two distinct phases can emerge, depending on the relative magnitudes of gain/loss and coupling strength. Specifically, the system can be in either the PT-symmetric phase (unbroken PT symmetry phase) or the broken PT-symmetric phase. In the PT-symmetric phase, the eigenvalues are real, and energy is equally distributed between the transmitter (Tx) and receiver (Rx) resonators. As a result, the output power and transfer efficiency remain unaffected by variations in the coupling coefficient. In the broken PT-symmetric phase, the eigenvalues become complex, and the output power and transfer efficiency can no longer be maintained due to the imbalance between gain and loss. The transition between these two phases occurs at a critical point called the exceptional point (EP). As the system's parameters, such as gain/loss or coupling strength, are varied, the system can switch from one phase to another.

As noted, maintaining the balance between gain and loss is crucial for preserving PT symmetry in a system. In [1], nonlinear saturation gain element was introduced to the PT-symmetric WPT system to counterbalance the energy dissipation. The nonlinear gain is realized through an operational amplifier (op-amp) topology, and self-selection of the operating frequency optimizes the system performance. In response to the low transfer power and efficiency, [2] improved the op-amp topology to achieve more efficient power transfer. Furthermore, the switch-mode implementation, such as class E power amplifiers (PAs) [3], [4], half-bridge inverters [5], and full-bridge inverters [6], enables kilowatt-level power transfer, due to the use of high-power semiconductor devices. These methods generate nonlinear saturation gain by using the current in the Tx resonator as a feedback signal. As the coupling coefficient varies, the switching frequency can automatically adjust to maintain the

Received 19 May 2025; revised 1 August 2025; accepted 28 August 2025. Date of publication 1 September 2025; date of current version 22 October 2025. This work was supported in part by the research funds for the National Natural Science Foundation of China under Grant 52277003 and in part by the Fundamental Research Funds for the Central Universities under Grant 2024CDJXY027. Recommended for publication by Associate Editor O. L. Lucia. *(Corresponding author: Xin Dai.)*

Ruozhong Gao, Xin Dai, and Shijun Zhao are with the School of Automation, Chongqing University, Chongqing 400044, China (e-mail: Gaoruozhong@cqu.edu.cn; daixin@cqu.edu.cn; zsjwpt@cqu.edu.cn).

Pengqi Deng is with the College of Optoelectronics Engineering, Chongqing University of Posts and Telecommunications, Chongqing 400065, China (e-mail: dengpq@cqupt.edu.cn).

Jinde Wu is with the School of Electrical and Power Engineering, Taiyuan University of Technology, Shanxi 030024, China (e-mail: wujinde@tyut.edu.cn).

Yanling Li is with the School of Electrical Engineering and Electronic Information, Xihua University, Chengdu 610039, China (e-mail: yanling.li@mail.xhu.edu.cn).

Color versions of one or more figures in this article are available at https://doi.org/10.1109/TPEL.2025.3605050.

Digital Object Identifier 10.1109/TPEL.2025.3605050

optimal energy transfer conditions. Compared to operational amplifiers, the saturation voltage in the switch-mode elements correspond to the dc supply voltage, thereby providing flexibility in controlling the power transfer.

Building on the realization of nonlinear gain, extensive studies have been conducted, focusing on compensation topologies [2], [6], [7], [8], [9], [10], [11], [12], [13], [14], such as double-transmitting coils, multiple repeaters, Rx-side series inductors, Series/Parallel-Series (S/PS) topology, Series/Series/Series-Parallel (S/S/SP) topology, and Single-Inductor-Double-Capacitor (SLDC) topology, as well as control schemes [16-23], such as phase shift control (PSC), pulse frequency modulation (PFM), and time-sharing control. These studies primarily aim to enhance power transfer capability, extend transmission distance, and improve power supply flexibility.

According to PT symmetry theory, the conditions required for PT-symmetric operation are stringent: the resonant frequencies of the transmitter Tx and Rx must be precisely matched. However, capacitance drift–caused by thermal fluctuations, aging, and manufacturing tolerances–leads to detuning between the Tx and Rx resonators. For instance, multilayer ceramic capacitors (MLCCs), except for NP0 types, exhibit significant capacitance drift, often exceeding 10% due to temperature variations [28]. In addition, the manufacturing tolerances of MLCCs and film capacitors typically range from $\pm 5\%$ to $\pm 10\%$ [29]. These factors can disrupt the PT-symmetric condition and severely degrade system performance.

Furthermore, eigenfrequency bifurcation caused by parameter variations (e.g., changes in coupling coefficient and load conditions) can induce significant frequency deviations. Eigenstate transitions triggered by stochastic perturbations (e.g., slight detuning of the resonators) can further exacerbate this behavior [1]. These frequency fluctuations not only limit design flexibility, given the strict operating bands defined by regulatory standards, but also complicate filter design across various subsystems, including signal processing stages, impedance matching networks, and electromagnetic interference suppression.

To date, these issues have received limited attention. This article proposes a straightforward method to achieve fixed-frequency PT-symmetric operation using dual-side synchronous series compensators (SSCs). While some recent dual-side tuning studies have focused on power regulation [30], [31], [32], [33], [34], most rely on multiloop control architectures, which add to overall system complexity. Moreover, such designs typically require interloop coordination to avoid issues such as bandwidth mismatch and timing conflicts. In this work, by maintaining PT symmetry consistently via a single control loop, the system can autonomously converge to a steady state. The proposed method requires active control only on the Rx-side SSC, while the Tx-side SSC operates autonomously via a predefined phase relationship. Specifically, by maintaining a $\pi/2$ phase shift between the Tx-side SSC and the inverter voltage, and dynamically adjusting the phase of the Rx-side SSC, balanced energy distribution between the Tx and Rx resonators is achieved at a fixed frequency. Phase determination requires neither coupling coefficient estimation nor wireless communication; the control angle is derived directly from output voltage and current measurements. For practical implementation, an auxiliary measurement coil (AMC) and a decoupling transformer (DT) are integrated to extract the synchronization signal from the Tx side, enabling phase alignment. Compared with conventional PT-symmetric realizations, the main advantages of the proposed method are as follows:

1) The output voltage and transfer efficiency are robust to variations in self-inductance, coupling coefficient, and load, while also demonstrates strong robustness to compensation capacitance drift, allowing the use of capacitors with larger tolerances;
2) PT-symmetric operation is achieved at a fixed frequency, thereby mitigating potential issues caused by large frequency variations;
3) Zero-voltage switching (ZVS) operation can be achieved across the entire operating range by adding an appropriate inductor in parallel at the inverter output.

The rest of this article is organized as follows. Section II discusses the PT-symmetric conditions for the dual-side active tuning system. Section III reviews the characteristics of the SSC and outlines the configuration of the system with dual SSCs. Section IV details the implementation of the fixed-frequency PT-symmetric system. Section V presents the experimental results and a comparison with existing works. Finally, Section VI concludes this article.

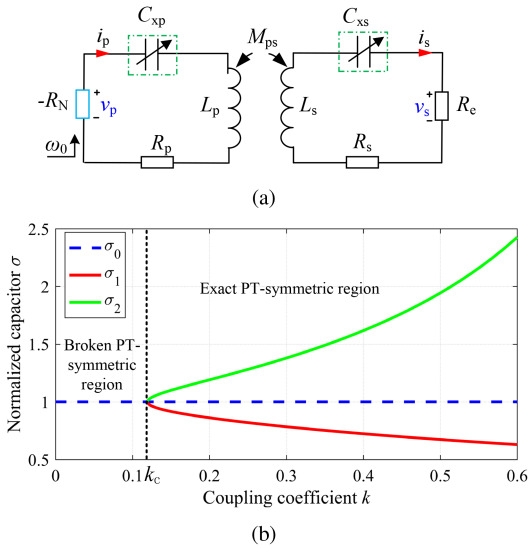

Fig. 1. (a) Equivalent circuit of the dual-side active tuning WPT system. (b) Normalized capacitance as the coupling coefficient changes.

II. Theoretical Analysis

A. PT-Symmetric Condition for Dual-Side Active Tuning System

The equivalent circuit of the dual-side active tuning system is as shown in Fig. 1(a). According to the definition of PT

symmetry, it can be known that the system satisfies the PT symmetry condition if $L_\mathrm{p} = xL_\mathrm{s}$, $C_\mathrm{p} = L_\mathrm{s}/x$, and $R_\mathrm{N} - R_\mathrm{p} = x(R_\mathrm{s} + R_\mathrm{e})$. Here, L_p and L_s represent the inductance of the Tx and Rx coils, respectively. C_xp and C_xs are the corresponding compensating capacitors, and R_p and R_s are the corresponding equivalent series resistances (ESRs). M_ps represents the mutual inductance between L_p and L_s. R_e represents the equivalent load, responsible for consuming the output power, while $-R_\mathrm{N}$ represents the negative resistor that provides the necessary gain to balance the gain and loss. ω_0 is the resonant angular frequency and satisfies

$$\omega_0 = 2\pi f_0 = \frac{1}{\sqrt{L_\mathrm{p}C_\mathrm{p}}} = \frac{1}{\sqrt{L_\mathrm{s}C_\mathrm{s}}} \tag{1}$$

where C_p and C_s represent the resonant capacitances for L_p and L_s, respectively. Let σ be the normalized capacitance, then the following relationship can be obtained:

$$\sigma = \frac{C_\mathrm{xp}}{C_\mathrm{p}} = \frac{C_\mathrm{xs}}{C_\mathrm{s}}. \tag{2}$$

Assuming the system's operating frequency remains constant at ω_0, the mathematical model of Fig. 1(a) can be expressed as

$$\begin{bmatrix} \omega_0 C_\mathrm{p}(R_\mathrm{p}-R_\mathrm{N})+\mathrm{j}\dfrac{\sigma-1}{\sigma} & \mathrm{j}\sqrt{\dfrac{C_\mathrm{p}}{C_\mathrm{s}}}k_\mathrm{ps} \\ \mathrm{j}\sqrt{\dfrac{C_\mathrm{s}}{C_\mathrm{p}}}k_\mathrm{ps} & \omega_0 C_\mathrm{s}(R_\mathrm{e}+R_\mathrm{s})+\mathrm{j}\dfrac{\sigma-1}{\sigma} \end{bmatrix} \begin{bmatrix} \boldsymbol{I}_\mathrm{p} \\ \boldsymbol{I}_\mathrm{s} \end{bmatrix} = 0 \tag{3}$$

where $\boldsymbol{I}_\mathrm{p}$ and $\boldsymbol{I}_\mathrm{s}$ represent the phasors of the Tx current i_p and Rx current i_s, respectively.

The normalized capacitance σ can be obtained by the characteristic equation, which can be expressed as follows by separating the imaginary and real parts:

$$\begin{cases} \dfrac{\omega_0(\sigma-1)\left[C_\mathrm{p}(R_\mathrm{p}-R_\mathrm{N})+C_\mathrm{s}(R_\mathrm{e}+R_\mathrm{s})\right]}{\sigma} = 0 \\ k_\mathrm{ps}^2 + C_\mathrm{p}C_\mathrm{s}(R_\mathrm{p}-R_\mathrm{N})(R_\mathrm{e}+R_\mathrm{s})\omega_0^2 - \dfrac{(\sigma-1)^2}{\sigma^2} = 0. \end{cases} \tag{4}$$

The real steady solutions can be derived as

$$\sigma = \begin{cases} \sigma_0 = 1 \\ \sigma_{1,2} = \dfrac{1}{1 \pm \sqrt{k_\mathrm{ps}^2 - \omega_0^2 C_\mathrm{s}^2 (R_\mathrm{e}+R_\mathrm{s})^2}}, \quad k_c \le k_\mathrm{ps} \le 1 \end{cases} \tag{5}$$

where k_c is the critical coupling coefficient which is given by

$$k_\mathrm{c} = \omega_0 C_\mathrm{s}\left(R_\mathrm{e}+R_\mathrm{s}\right). \tag{6}$$

The mathematical results are plotted in Fig. 1(b). The real steady solutions can be categorized into two regions: 1) when $k_\mathrm{ps} < k_\mathrm{c}$, there is one real solution σ_0, and the system operates in the broken PT-symmetric region; 2) when $k_\mathrm{ps} \ge k_\mathrm{c}$, there are two additional real solutions σ_1 and σ_2, and the system can operate in the exact PT-symmetric region.

B. Transmission Characteristics

1) Exact PT-symmetric Region: when $k_\mathrm{ps} \ge k_\mathrm{c}$, the system operates at either σ_1 or σ_2, satisfying the PT-symmetric conditions. In this case, the negative resistance $-R_\mathrm{N}$ can be derived from (4) as

$$-R_\mathrm{N} = \frac{-C_\mathrm{s}\left(R_\mathrm{e}+R_\mathrm{s}\right)}{C_\mathrm{p}} - R_\mathrm{p}. \tag{7}$$

Combining (7) and (3), the current ratio can be obtained as

$$\frac{I_\mathrm{s}}{I_\mathrm{p}} = \frac{\sqrt{C_\mathrm{s}}}{\sqrt{C_\mathrm{p}}} \tag{8}$$

where I_p and I_s are the root-mean-square (RMS) values of i_p and i_s, respectively.

Then, the voltage gain can be given by

$$\frac{V_\mathrm{s}}{V_\mathrm{p}} = \frac{I_\mathrm{s}R_\mathrm{e}}{I_\mathrm{p}R_N} = \frac{\sqrt{C_\mathrm{p}C_\mathrm{s}}R_\mathrm{e}}{C_\mathrm{p}R_\mathrm{p} + C_\mathrm{s}\left(R_\mathrm{s}+R_\mathrm{e}\right)} \tag{9}$$

where V_p and V_s are the RMS values of v_p (the voltage across the negative resistance) and v_s (the voltage across the load resistance), respectively. The transfer efficiency can be derived as

$$\eta = \frac{I_\mathrm{s}V_\mathrm{s}}{I_\mathrm{p}V_\mathrm{p}} = \frac{C_\mathrm{s}R_\mathrm{e}}{C_\mathrm{s}R_\mathrm{e} + C_\mathrm{p}R_\mathrm{p} + C_\mathrm{s}R_\mathrm{s}}. \tag{10}$$

Furthermore, according to (9), the output power P_o can be expressed as

$$P_\mathrm{o} = \frac{V_\mathrm{s}^2}{R_\mathrm{e}} = \frac{C_\mathrm{p}C_\mathrm{s}R_\mathrm{e}V_\mathrm{p}^2}{\left[C_\mathrm{p}R_\mathrm{p} + C_\mathrm{s}\left(R_\mathrm{e}+R_\mathrm{s}\right)\right]^2}. \tag{11}$$

It can be observed from (9) and (11) that in the exact PT-symmetric region, the transfer efficiency and the output power are independent of the coupling coefficient. This means that as the coupling coefficient changes, the capacitors C_xp and C_xs can be simultaneously adjusted to maintain stable output voltage and transfer efficiency while keeping the operating frequency at ω_0.

2) Broken PT-symmetric Region: when $k_\mathrm{ps} < k_\mathrm{c}$, the system operates at σ_0, and the PT-symmetry is broken. In this case, the negative resistance can be derived from (4) as

$$-R_N = \frac{k_\mathrm{ps}}{-\omega_0^2 C_\mathrm{p}C_\mathrm{s}\left(R_\mathrm{e}+R_\mathrm{s}\right)} - R_\mathrm{p}. \tag{12}$$

Similarly, the current ratio and voltage gain can be derived as

$$\begin{cases} \dfrac{I_\mathrm{s}}{I_\mathrm{p}} = \dfrac{k_\mathrm{ps}}{\omega_0\sqrt{C_\mathrm{p}C_\mathrm{s}}(R_\mathrm{e}+R_\mathrm{s})} \\ \dfrac{V_\mathrm{s}}{V_\mathrm{p}} = \dfrac{\omega_0 k_\mathrm{ps}\sqrt{C_\mathrm{p}C_\mathrm{s}}R_\mathrm{e}}{k^2 + \omega_0^2 C_\mathrm{p}C_\mathrm{s}R_\mathrm{p}(R_\mathrm{e}+R_\mathrm{s})}. \end{cases} \tag{13}$$

Then the transfer efficiency and the output power can be derived as

$$\begin{cases} \eta = \dfrac{I_\mathrm{s}V_\mathrm{s}}{I_\mathrm{p}V_\mathrm{p}} = \dfrac{k_\mathrm{ps}^2 R_\mathrm{e}}{\left(R_\mathrm{e}+R_\mathrm{s}\right)\left[k_\mathrm{ps}^2 + \omega_0^2 C_\mathrm{p}C_\mathrm{s}R_\mathrm{p}(R_\mathrm{e}+R_\mathrm{s})\right]} \\ P_\mathrm{o} = \dfrac{V_\mathrm{s}^2}{R_\mathrm{e}} = \dfrac{\omega_0^2 k_\mathrm{ps}^2 C_\mathrm{p}C_\mathrm{s}R_\mathrm{e}V_\mathrm{p}^2}{\left[k_\mathrm{ps}^2 + \omega_0^2 C_\mathrm{p}C_\mathrm{s}R_\mathrm{p}(R_\mathrm{e}+R_\mathrm{s})\right]^2}. \end{cases} \tag{14}$$

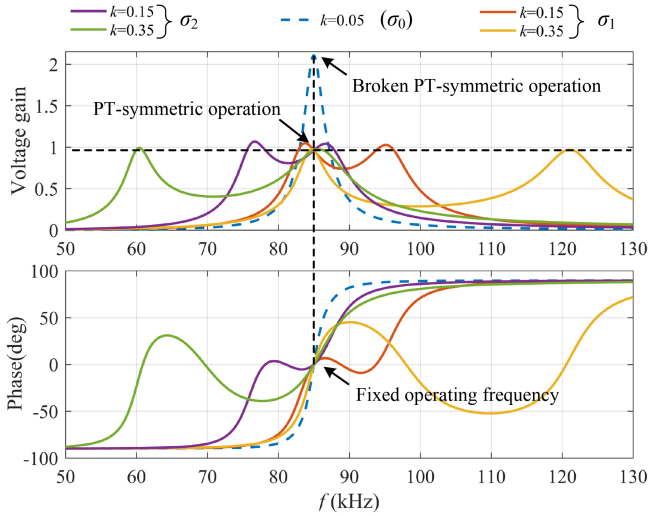

Fig. 2. Voltage gain and input impendence angle of the circuit under different coupling coefficients with variable σ, where $k_c = 0.119$.

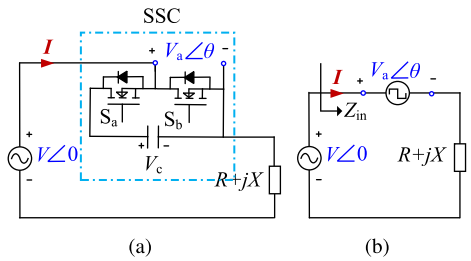

Fig. 3. (a) Basic circuit with SSC. (b) Its equivalent circuit.

As can be seen from (14), when the system operates in the weak coupling region ($k_{ps} < k_c$), both the output power and transfer efficiency vary with the coupling coefficient. In this region, the compensation capacitance on both sides are always equal to C_p and C_s, respectively, i.e., $\sigma_0 = 1$.

Fig. 2 presents the voltage gain and input impendence angle of the system under the conditions $L_p = L_s = 80\,\mu$H, $\omega_0 = 2\pi \times 85$ kHz, $R_p = R_s = 0.1\,\Omega$, and $R_e = 5\,\Omega$. As shown in this figure, when $k_{ps} \geq k_c$ (e.g., $k_{ps} = 0.15$ and $k_{ps} = 0.35$), there exists two values of σ that can compensate for the additional reactance in the circuit, allowing the system to operate in the exact PT-symmetric region at a fixed switching frequency of ω_0. Conversely, when $k_{ps} < k_c$ (e.g., $k_{ps} = 0.05$), the real solution for σ becomes 1, indicating that the system operates in the broken PT-symmetric region.

In summary, operation at σ_1 and σ_2 is preferred because it ensures consistent output voltage and transfer efficiency when displacement occurs between the Tx and Rx.

III. PT-Symmetric WPT System With a Fixed Operating Frequency Using Dual SSCs

In this section, active reactance compensators, referred to as automatic tuning assist circuits [24] or SCC [25], are introduced to facilitate the operation of the PT-symmetric WPT system. Fig. 3(a) shows the basic circuit with SSC. The SSC comprises a half-bridge inverter and a filter capacitor, and the duty cycle of the half-bridge inverter is always 50%. $V\angle 0$ represents a sinusoidal voltage source. $R + \mathrm{j}X$ represents the load impedance, including the real (resistive) and imaginary (reactive) components. Assume that the filter capacitor is sufficiently large so that the voltage across the capacitor (V_c) remains constant in the steady state. Therefore, it can be approximated as a constant voltage source, and the circuit can be simplified as shown in Fig. 3(b). The output voltage of the inverter leads $V\angle 0$ by θ, denoted as $V_a\angle\theta$. The current $\boldsymbol{I}$ can be calculated as

$$\boldsymbol{I} = \frac{V - V_a\left(\cos\theta + \mathrm{j}\sin\theta\right)}{R + jX}. \tag{15}$$

It is evident that the source $V_a\angle\theta$ stores and releases energy rather than dissipating it, hence

$$\mathrm{Re}\left(\bar{S}_{SSC}\right) = 0 \tag{16}$$

where $\bar{S}_{SSC}$ represents the complex power of the SSC. Combing (15) and (16) yields

$$V_a = \frac{V\left(R\cos\theta - X\sin\theta\right)}{R}. \tag{17}$$

The equivalent impendence of the SSC can be derived as

$$Z_a = \frac{V_a\left(\cos\theta + \mathrm{j}\sin\theta\right)}{\boldsymbol{I}}. \tag{18}$$

Substituting (15) and (17) into (18) yields

$$Z_a = -j\left(X - R\cot\theta\right). \tag{19}$$

Equation (19) demonstrates that adjusting the angle θ can modify the equivalent impedance of the SSC. Specifically, when $\theta = \pm\pi/2$, the equivalent impedance becomes $-\mathrm{j}X$. This means that the SSC can fully cancel the reactive component $\mathrm{j}X$, whether capacitive or inductive. In practical applications, V_c must be ensured as nonnegative due to the antiparallel diodes in MOSFETs. Therefore, the drive signals for S_a and S_b should be reversed when this condition arises. Fig. 4 shows the key waveforms of the circuit during the tuning process at $\theta = \pm\pi/2$. The red area represents the capacitor charging region, and the blue area represents the capacitor discharging region. The charging area

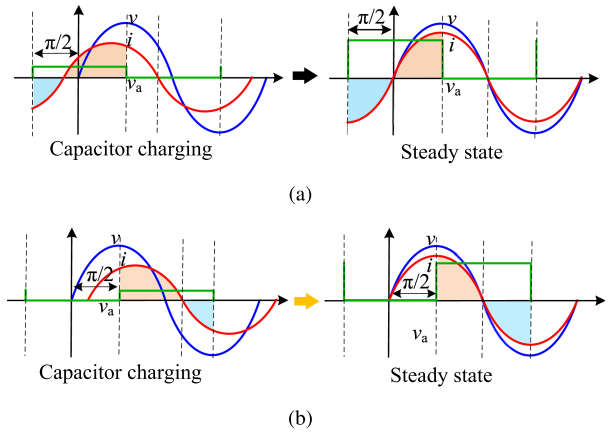

Fig. 4. Key waveforms during the tuning process. (a) SSC behaves inductively. (b) SSC behaves capacitively.

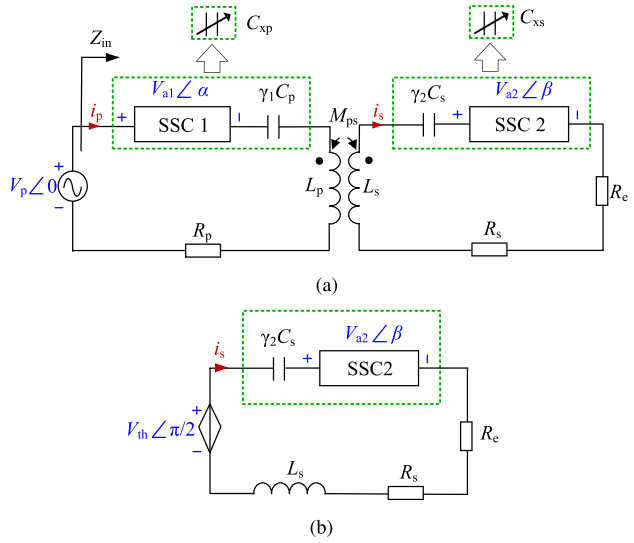

Fig. 5. (a) Main circuit diagram of the dual-side active tuning system. (b) Equivalent circuit, where the induced voltage v_{th} leads v_p by $\pi/2$ when $\alpha = \pm\pi/2$.

cannot be less than the discharging area. Consequently, θ should be $\pi/2$ when the SSC exhibits capacitance, and $-\pi/2$ when the SSC exhibits inductance.

The proposed system with dual SSCs is shown in Fig. 5(a). The input voltage phase is considered the reference zero phase, denoted as $V_p\angle 0$. The voltages across SSC1 and SSC2 are denoted as $V_{a1}\angle\alpha$ and $V_{a2}\angle\beta$, respectively. $\gamma_1 C_p$ and $\gamma_2 C_s$ represent the series compensating capacitors on the Tx and Rx sides, respectively, which can mitigate the voltage stress on the SSCs and suppress higher-order harmonics. Here, γ_1 and γ_2 represent their respective normalized capacitance values. $\gamma_1 C_p$ and SSC1 constitute the variable capacitor C_{xp}, while $\gamma_2 C_s$ and SSC2 constitute the variable capacitor C_{xs}.

Based on the previous analysis, irrespective of the reflected impedance, if α is equal to $\pi/2$ or $-\pi/2$, v_p and i_p will naturally be in phase in the steady state. Consequently, the induced voltage on the Rx side leads i_p by $\pi/2$, denoted as $V_{th}\angle\pi/2$. The equivalent circuit of the Rx side is shown in Fig. 5(b), and the equivalent reactance of SSC2 can be derived as

$$Z_{a2} = -\mathrm{j}\left[\left(1-\frac{1}{\gamma_2}\right)\omega_0 L_s + (R_s+R_e)\tan\beta\right]. \tag{20}$$

C_{xs} can be expressed as

$$C_{xs} = \frac{1}{\omega_0^2 L_s + \omega_0 (R_s+R_e)\tan\beta}. \tag{21}$$

Combining (21) and (5) yields

$$\frac{1}{\omega_0^2 L_s + \omega_0 (R_s+R_e)\tan\beta} = \sigma C_s. \tag{22}$$

By solving (22), β can be derived as

$$\beta = \begin{cases} \beta_0 = 0 \\ \beta_{1,2} = \pm\arctan\sqrt{\dfrac{k_{ps}^2}{\omega_0^2 C_s^2 (R_e+R_s)^2} - 1}, \end{cases} \quad k_{ps} \geq k_c. \tag{23}$$

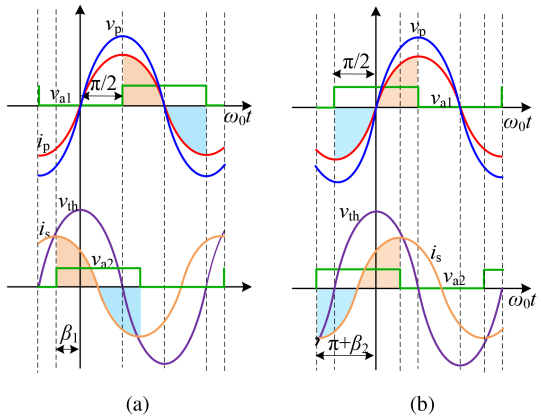

Fig. 6. Key waveforms of the dual-side active tuning system. (a) The system operates at σ_1 (i.e., $\beta = \beta_1$). (b) The system operates at σ_2 (i.e., $\beta = \beta_2$).

When $k_{ps} \geq k_c$, there are three real solutions (β_0, β_1, and β_2), among which β_1 and β_2 correspond to the phase angles that allow the system to operate within the PT-symmetric region. Conversely, when $k_{ps} < k_c$, the real solutions degenerate to 1, and the system operates in the broken PT-symmetric region. Besides, according to (23), β have no relation to γ_1 and γ_2, which means that precise values for the series-compensation capacitors are not required.

As shown in Fig. 6(a) and (b), the following conditions ensure the correct operation of the SSCs: 1) when operating at σ_1 (i.e., $\beta = \beta_1$), v_{a1} should lag v_p by $\pi/2$, and v_{a2} should lead v_p by β_1; 2) when operating at σ_2 (i.e., $\beta = \beta_2$, where $\beta_2 < 0$), v_{a1} should lead v_p by $\pi/2$, and v_{a2} should lead v_p by $\pi/2 + \beta_2$.

Both SSCs exhibit capacitive behavior at σ_1 and behavior inductive at σ_2. Therefore, γ_1 and γ_2 should meet

$$\begin{cases} \gamma_{1,2} \geq \sigma_1, & \text{when } \beta = \beta_1 \\ \gamma_{1,2} \leq \sigma_2, & \text{when } \beta = \beta_2. \end{cases} \tag{24}$$

This means that when $\beta = \beta_1$, γ_1 and γ_2 should be at least the maximum value of σ_1; whereas when $\beta = \beta_2$, γ_1 and γ_2 should not exceed the minimum value of σ_2. Assuming that k_{min} is the minimum coupling coefficient ($k_{min} \geq k_c$), combining (5) and (24), we obtain

$$\begin{cases} \gamma_{1,2} \geq \dfrac{1}{1+\sqrt{k_{min}^2 - \omega_0^2 C_s^2 (R_e+R_s)^2}}, & \text{when } \beta = \beta_1, \\ \gamma_{1,2} \leq \dfrac{1}{1-\sqrt{k_{min}^2 - \omega_0^2 C_s^2 (R_e+R_s)^2}}, & \text{when } \beta = \beta_2. \end{cases} \tag{25}$$

In particular, when $k_{min} = k_c = \omega_0 C_s (R_e + R_s)$, the following conditions hold:

$$\begin{cases} \gamma_{1,2} \geq 1, & \text{when } \beta = \beta_1 \\ \gamma_{1,2} \leq 1, & \text{when } \beta = \beta_2. \end{cases} \tag{26}$$

IV. System Implementation

A. Overview of the Proposed System

Fig. 7(a) illustrates the schematic diagram of the system with control modules. Power is provided by a full-bridge inverter and

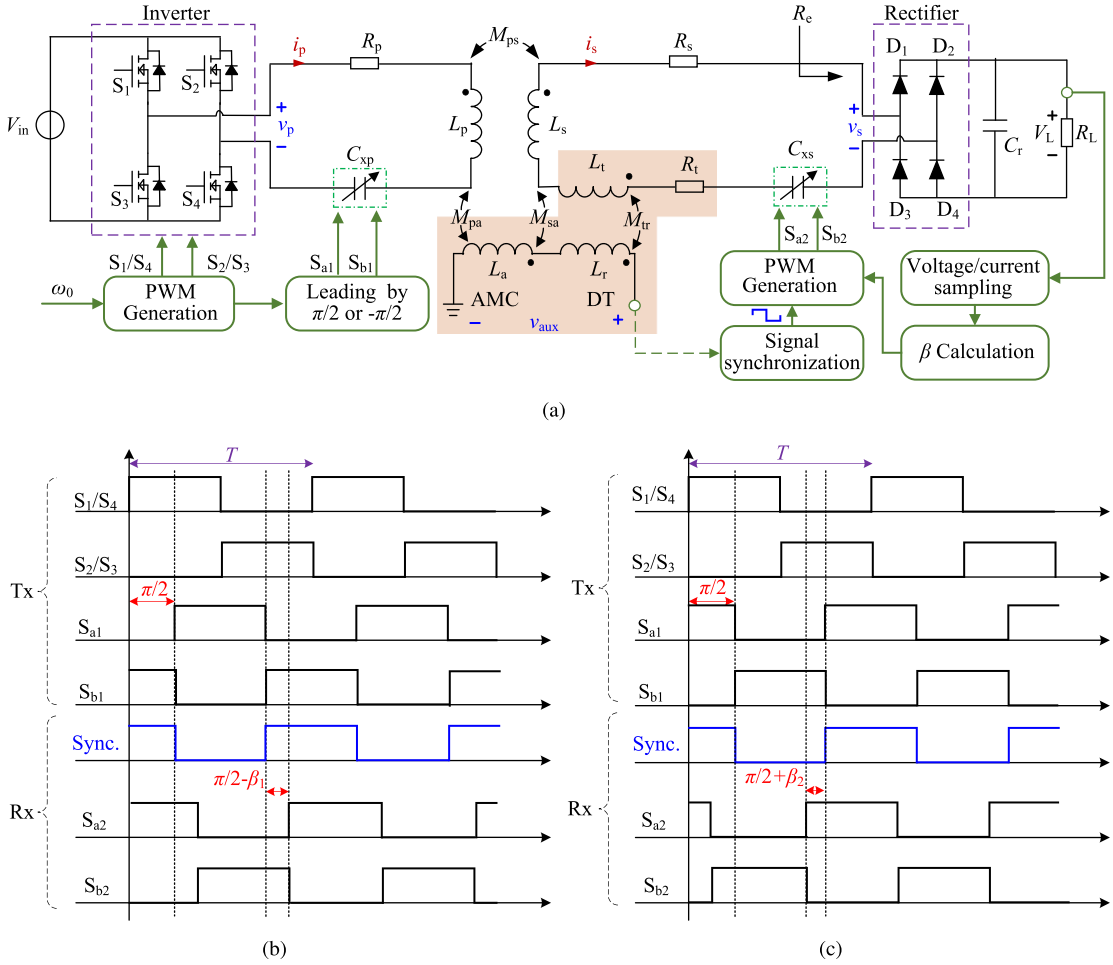

Fig. 7. (a) Overview of the proposed system. (b) Drive signals when the system operates at σ_1 (i.e., $\beta = \beta_1$). (c) Drive signals when the system operates at σ_2 (i.e., $\beta = \beta_2$).

received by a full-bridge rectifier. By applying fundamental harmonic analysis and the energy conservation law, the following relationships can be derived [25]:

$$V_{\mathrm{p}} = \frac{2\sqrt{2}}{\pi} V_{\mathrm{in}}, V_{\mathrm{s}} = \frac{2\sqrt{2}}{\pi} V_{\mathrm{L}}, R_{\mathrm{e}} = \frac{8R_{\mathrm{L}}}{\pi^2} \tag{27}$$

where V_{in} is the input dc voltage of the inverter, R_{L} is the dc load at the end of the rectifier, and V_{L} is the voltage across R_{L}. In this system, S_1 to S_4 represent the drive signals for the full-bridge inverter, which are fixed at ω_0. S_{a1} and S_{b1} represent the drive signals for SSC1, while S_{a2} and S_{b2} represent the drive signal for SSC2.

B. Control Scheme

Based on the prior analysis, achieving PT-symmetric operation requires the simultaneous adjustment of the SSCs on the Tx and Rx sides. The timing diagram of the drive signals is depicted in Fig. 7(b) and (c). When S_{a1} lags or leads S_1 by $\pi/2$, v_{a1} will naturally lag or lead v_{p} by $\pi/2$. This is readily achievable since a controller on the Tx side can generate the drive signals for both the inverter and SSC1.

There are two key issues for SSC2

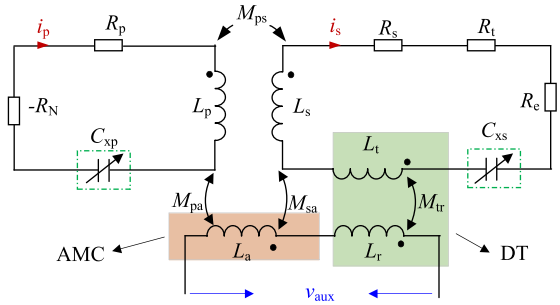

Fig. 8. System with an AMC and DT.

1) Tx Synchronization Signal: An AMC on the Rx side can be utilized to capture the Tx synchronization signal [26], [27]. The circuit is shown in Fig. 8. The mutual inductances of the AMC with the Tx and Rx coils are denoted as M_{pa} and M_{sa}, respectively. A DT is employed to decouple the AMC from the Rx coil, with the mutual inductance M_{tr} between its two windings. The first harmonic induced voltage across the AMC can be calculated as

$$V_{\mathrm{aux}} = j\omega_0 M_{\mathrm{pa}} \boldsymbol{I}_{\mathrm{p}} + j\omega_0 \left(M_{\mathrm{sa}} - M_{\mathrm{tr}}\right) \boldsymbol{I}_{\mathrm{s}}. \tag{28}$$

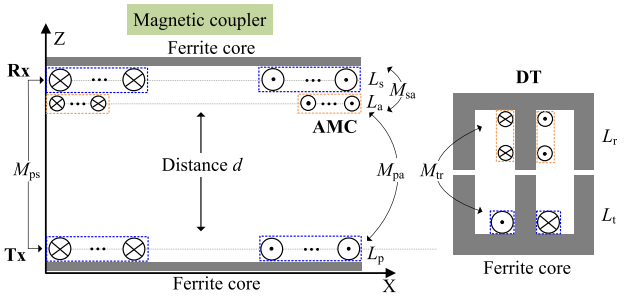

Fig. 9. Structure of the AMC and decoupling transformer.

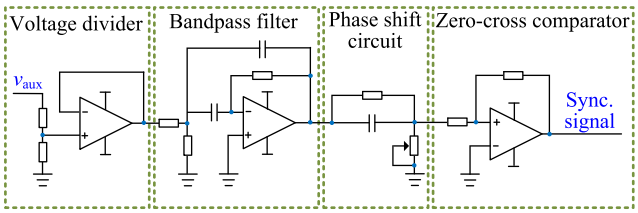

Fig. 10. Scheme of the synchronization circuit.

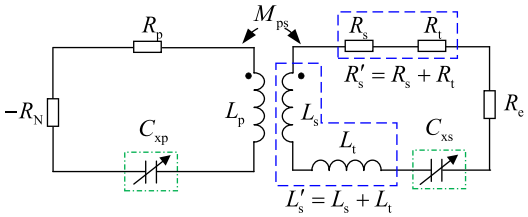

Fig. 11. Scheme of the synchronization circuit.

If M_{sa} is equal to M_{tr}, the voltage induced by L_s is expected to be canceled by the DT, resulting in v_{aux} leading i_p by $\pi/2$. Since i_p is in phase with v_p in the steady state, v_{aux} naturally leads v_p by $\pi/2$. As a result, S_{a2} only needs to lag v_{aux} by $\pi/2-\beta_1$ (when operating at σ_1) or lead it by $\pi/2+\beta_2$ (when operating at σ_2), as illustrated in Fig. 7(b) and (c). The structure of the AMC and DT is shown in Fig. 9. The AMC is positioned on the plane of the Rx coil and connected in series with the secondary winding of the DT, while the Rx coil is connected in series with the primary winding. Since the AMC is open-circuited, it can be wound with thin wire, saving both space and weight.

The synchronization signal detection is implemented based on the scheme illustrated in Fig. 10. The induced voltage is conditioned, passed through a bandpass filter to eliminate higher-order harmonics, phase-corrected, and finally sent through a hysteresis comparator to output the synchronization signal to the controller.

To align with the theoretical analysis presented in Sections II and III, the main circuit can be equivalently represented by the circuit shown in Fig. 11 and has

$$\begin{cases} R'_s = R_s + R_t \\ L'_s = L_s + L_t \\ k'_{ps} = k_{ps}\sqrt{1-\omega_0^2 C_s L_t} \end{cases} \tag{29}$$

TABLE I
MATHEMATICAL RESULTS

Parameter	Expressions
k_c	$\dfrac{\omega_0 C_s(R_t+R_s+R_e)}{\sqrt{1-\omega_0^2 C_s L_t}}$
$\sigma_{1,2}$	$\dfrac{1}{1\pm\sqrt{{k_{ps}}^2(1-\omega_0^2 C_s L_t)-\omega_0^2 C_s^2(R_e+R_s+R_t)^2}}$
$\beta_{1,2}$	$\pm\arctan\sqrt{\dfrac{k_{ps}^2(1-\omega_0^2 C_s L_t)}{\omega_0^2 C_s^2(R_e+R_s+R_t)^2}-1}$
P_o	$\dfrac{C_p C_s R_e V_p^2}{[C_p R_p + C_s(R_e+R_s+R_t)]^2}$
η	$\dfrac{C_s R_e}{C_s R_e + C_p R_p + C_s(R_s+R_t)}$

*Note that: $C_s = 1/(\omega_0^2 L'_s)$.

By replacing R_s, L_s, and k_{ps} in Sections II and III with R'_s, L'_s, and k'_{ps}, we can obtain the corresponding expressions for Fig. 11. It should be noted that L_t typically consists of only a few turns, resulting in very small losses. For convenience, key results are summarized in Table I.

2) Values of β: For a given β (denoted as β_{given}), the input impendence of the system can be expressed as

$$Z_{in} = R_p + \frac{\left(\pi\omega_0 k_{ps}\sqrt{L_p L_s}\cos\beta_{given}\right)^2}{\pi^2(R_s+R_e)+8R_L}. \tag{30}$$

Then, the induced voltage on the Rx side can be given by

$$V_{th} = j\frac{2\sqrt{2}\,\omega_0 k_{ps}\sqrt{L_p L_s}\,V_{in}}{\pi Z_{in}}. \tag{31}$$

The dc output voltage is expressed as

$$V_L = \frac{\pi}{2\sqrt{2}}\left|\frac{8R_L V_{th}}{\left[\pi^2(R_s+R_e+R_t)+8R_L\right](1-j\tan\beta_{given})}\right|. \tag{32}$$

By solving (32), the coupling coefficient k_{ps} can be obtained as

$$k_{ps} = \frac{\omega_0\sqrt{C_p C_s\left[32A^2 - BV_L^2 + 8A\sqrt{16A^2-BV_L^2}\right]}}{\pi^2 V_L\cos\beta_{given}\sqrt{1-\omega_0^2 C_s L_t}} \tag{33}$$

where

$$\begin{cases} A &= R_L V_{in}, \\ B &= \pi^2 R_p\left(8R_L+\pi^2 R_s+\pi^2 R_t\right). \end{cases} \tag{34}$$

Given that $C_p = 1/(\omega_0^2 L_p)$ and $C_s = 1/[\omega_0^2(L_s+L_t)]$, substituting (33) into the formulas for $\beta_{1,2}$ in Table I, the target β can be obtained, as shown at the top of next page.

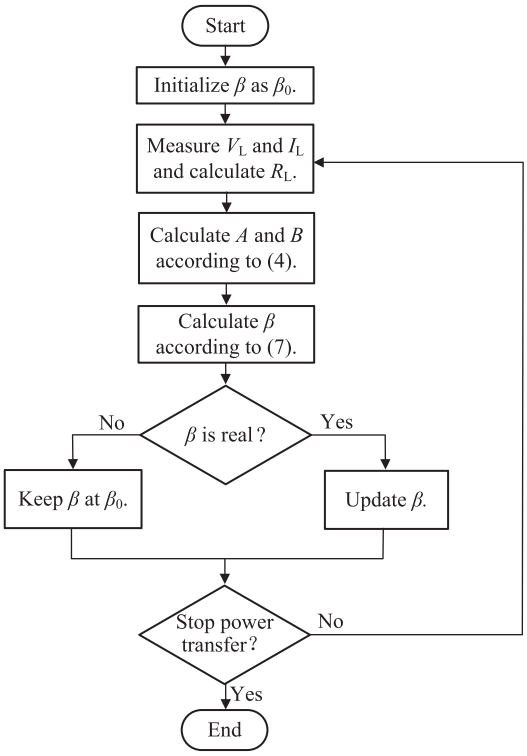

Fig. 12. Flowchart for determining the value of β.

Equation (35) shows that the optimal control angle β can be determined using a specified β_{given} and its corresponding measured output voltage V_L. Specifically, when the Tx and Rx coils are identical, the ratio $(L_s + L_t)/L_p$ remains approximately constant, irrespective of variations in L_p and L_s, due to the negligible value of L_t. Consequently, the calculation is largely unaffected by changes in the self-inductance.

Fig. 12 presents the flowchart for determining the value of β. Given an initial value β_0, the load R_L can be ascertained by measuring the load voltage V_L and current I_L. Using (34), coefficients A and B can be calculated, and subsequently, the target control angle β can be derived from (35). Note that when β is a real number, the system lies within the PT-symmetric region, and the control angle should be updated; otherwise, the system is in the PT-broken region, and the control angle remains at the initial value β_0. When the transmission distance or load changes, V_L and I_L are remeasured based on the control angle from the previous step to compute the new optimal angle.

C. Soft Switching of the System

1) Soft switching of Inverter: To achieve zero voltage switching (ZVS) of the inverter, switching devices must ensure that the voltage is close to zero during turn-ON. If the circuit impedance is weakly inductive, the voltage across the switching devices

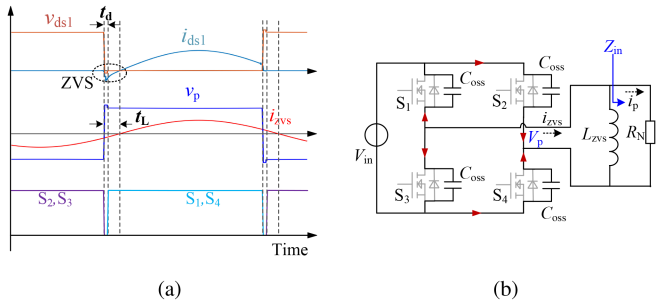

Fig. 13. Analysis of soft-switching of S_1 considering the dead time. (a) Key waveforms. (b) Equivalent circuit viewed from the Tx side during the dead time.

will drop to nearly zero before the they are turned ON due to the current freewheeling through the body diodes. Given that the input impedance Z_{in} is purely resistive and approximately equal to $R_N = (R_t + R_s + R_e)C_s/C_p + R_p$, adding an appropriate inductor L_{zvs} in parallel with the inverter output facilitates ZVS operation.

Fig. 13. illustrates the key waveforms and equivalent circuit during the dead time. For ZVS operation, it is essential to satisfy the condition $t_L \geq t_d$, where t_L is the time interval during which the inverter voltage leads the current and t_d is the dead time. During the dead time, the MOSFETs must maintain sufficient drain-source current to discharge their parasitic output capacitance, which is given by

$$Q_{ZVS} = \int_0^{t_d} |i_{ZVS}|\, dt \geq 2\int_0^{V_{in}} C_{oss} dv. \tag{36}$$

Assuming that the waveform of i_{zvs} within the dead time interval is a sine wave, it can be expressed as

$$\begin{aligned} i_{zvs} &= \frac{\sqrt{2}V_p}{R_N}\sin(\omega_0 t) - \frac{\sqrt{2}V_p}{\omega_0 L_{zvs}}\cos(\omega_0 t) \\ &= A_m \sin(\omega_0 t - \omega_0 t_L) \end{aligned} \tag{37}$$

where A_m represents the amplitude of i_{zvs}. Substituting (37) into (36), we can obtain

$$\frac{A_m\left[\cos\omega_0(t_d - t_L) - \cos\omega_0 t_L\right]}{\omega_0} \geq 2C_{oss}V_{in}. \tag{38}$$

To facilitate the calculation, let $t_L = t_d$. The range of L_{zvs} is derived as

$$L_{zvs} \leq L_{ZVS\_max} = \frac{2}{\sqrt{\pi\omega_0^3 C_{oss}\left(\pi\omega_0 C_{oss} + \frac{4}{R_N}\right)}}. \tag{39}$$

It can be seen from (39) that L_{zvs} has a positive correlation with R_N and a negative correlation with C_{oss}. To ensure ZVS across the entire operating condition range, L_{zvs} should be no greater than the minimum value of L_{zvs_max}, which can be determined

$$\beta_{1,2} = \pm\arctan\sqrt{\frac{(L_s + L_t)}{L_p}\cdot\frac{\pi R_p^2\left[32A^2 - BV_L^2 + 8A\sqrt{16A^2 - BV_L^2}\right]}{B^2 V_L^2\cos^2\beta_{\text{given}}} - 1}. \tag{35}$$

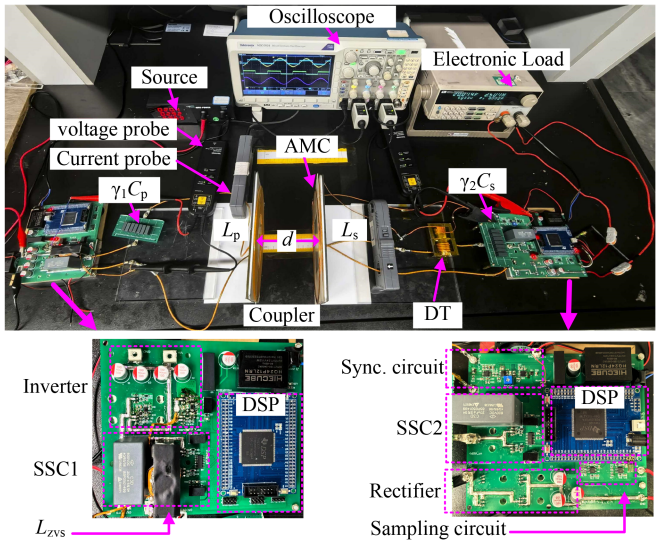

Fig. 14. Experimental prototype of the proposed system.

by substituting the maximum value of C_{oss} and the minimum value of R_N into (39).

According to (39), the power ratio between R_{zvs} and R_N can be derived as

$$P_{ratio} = \frac{P_{zvs}}{P_{R_N}} \approx \pi\omega_0 C_{oss} R_{zvs} + \left(\frac{\pi}{2}\omega_0 C_{oss}\right)^2 R_N R_{zvs} \quad (40)$$

where R_{zvs} represents the ESR of L_{zvs}. Since C_{oss} is generally very small, typically in the pF range, the power ratio is theoretically very low. In other words, the parallel inductor has a negligible impact on the system.

2) Soft switching of SCCs: When the Rx-side SSC operates at σ_1, both SSCs exhibit capacitive characteristics and achieve soft switching. Conversely, when the Rx-side SSC operates at σ_2, both SSCs exhibit inductive characteristics and lead to hard switching. Thus, it is preferred that the system operates at σ_1.

V. Experimental Verification

A. Experiment Setup

To validate the theoretical analysis and performance of the proposed system, an experimental prototype was developed, as shown in Fig. 14. The prototype comprises a dc voltage source, a full-bridge inverter, a magnetic coupler, two compensation capacitors, two SSCs, a full-bridge rectifier, an electronic load, and associated control circuits. The inverter employs four IRFB3607 MOSFETs, and each SSC contains two SCTWA90N65G2V-4 MOSFETs. The rectifier utilizes four MBR3060CT Schottky diodes. LM5106 and ADUM3223 are used to drive the inverter and SSCs, respectively. Digital signal processors (DSPs) TMS320F28335 are employed on both the Tx and Rx sides for design control. The magnetic coupler consists of two identical planar coils, wound with Litz wire, with a ferrite layer closely attached to the back of each coil for shielding and guiding the magnetic flux. Each coil has an outer diameter of 20 cm and consists of 19 turns. The mutual inductance M_{ps} between the Tx and Rx is measured using an LCR meter (HIOKI IM3536) while varying the distance from 5 cm to 14 cm. The key experimental parameters are listed in Table II.

TABLE II
Parameters for the Prototype

Parameter	Value	Parameter	Value
V_{in}	30 V	R_L	8–16 Ω
N_p	19	L_p	106.7–117.9 μH
N_s	19	L_s	106.3–118.1 μH
R_p	138 mΩ	R_s	134 mΩ
L_t	16.6 μH	R_t	25 mΩ
L_r	24.6 μH	L_a	7.6 μH
C_p	32.9 nF	C_s	28.0 nF
d	5 – 14 cm	ω_0	5.34×10^3 rad/s
M_{ps}	9.3 – 61.1 μH	k_{ps}	0.087–0.518
γ_1	1 and 1.143	γ_2	1 and 1.168

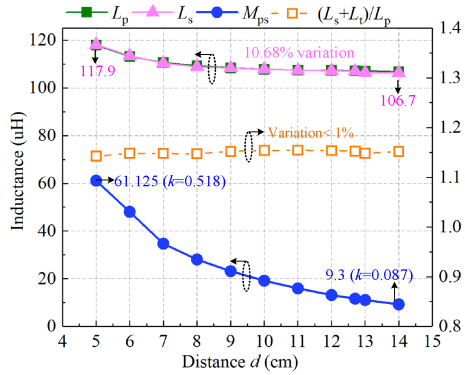

Fig. 15. Profile of the magnetic coupler parameters versus the transfer distance d.

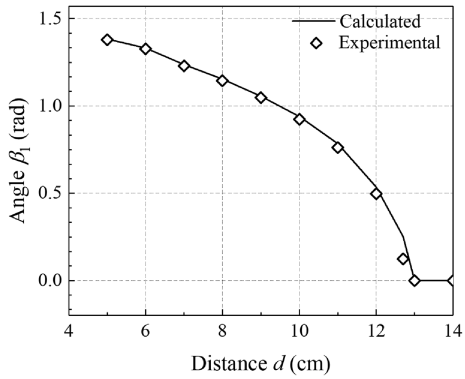

Fig. 16. Theoretical and experimental values of the optimal control angle β_1.

As illustrated in Fig. 15, with the increase in distance, the values of L_p and L_s ascend from about 106.7 μH to 117.9 μH. Meanwhile, M_{ps} decreases from around 61.1 μH to 9.3 μH, and the coupling coefficient k_{ps} drops from 0.518 to 0.087. As depicted in Fig. 16, even though there is a 10.68% variation in self-inductance, the ratio $(L_p + L_s)/L_p$ remains nearly constant at about 1.15 (with a change of less than 1%). The theoretical and experimental values of the optimal control angle exhibit good agreement.

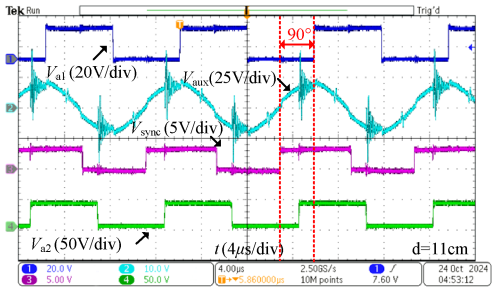

Fig. 17. Open circuit voltage in the measurement coil (V_{aux}) and the synchronization signal (V_{sync}).

In this experiments, γ_1 and γ_2 are designed to vary by 14.3% and 16.8%, respectively. It should be noted that the variation range for γ_1 and γ_2 could be extended, while increasing γ_1 and γ_2 results in a higher voltage across the SSCs. Due to the experimental limitations, only the values mentioned above are considered in this study.

B. Experiment Results

In this experiments, an ITECH IT8512 dc electronic load is employed. The currents and voltages are measured by the current probe (Cybertek CP8150 A) and voltage probe (Tektronix THDP0200), and recorded by a Tektronix Oscilloscope (Tektronix MDO3024).

1) Synchronization Signal Acquisition: Fig. 17 shows the open-circuit voltage across the AMC (V_{aux}) and the synchronization signal (V_{sync}) after signal conditioning, zero-crossing detection, and voltage level shifting. By detecting the rising edge of V_{sync}, the phase information of v_p can be directly obtained.

2) ZVS Operation of the Inverter: Since the switching behavior of the four MOSFETs in the inverter is similar, only the switching behavior of S_1 is illustrated for simplicity. Fig. 18(a) and (b) show the drain-source voltage (DS voltage) and gate-source signal (GS signal) of S_1, as well as the current I_{zvs} and I_p. As can be seen in the feagures, zero-phase angle (ZPA) and ZVS are achieved in the inverter, thereby reducing the losses.

3) Output Voltage and Efficiency of the System: Figs. 19(a) and 18(b) present the output voltage and efficiency of the proposed method at a load of 8 Ω as the distance d varies. In addition, experiments with the conventional method were conducted under the same conditions for comparison. Within the PT-symmetric region ($d < 12.7$ cm), the output voltage of the proposed method remains nearly constant, similar to that of the conventional method. Furthermore, the transfer efficiency of the proposed method stays above 90%. The slight reduction in efficiency at high coupling coefficients is mainly due to increased switching losses caused by the higher voltage across the SCCs. Figs. 20 and 21 illustrate the key waveforms of the system. The voltage across the Tx-side SCC (V_{a1}) is always 90° ahead of the inverter output voltage V_p. As the distance changes from 5 to 12 cm, the phase angle of the voltage across the Rx-side SCC (V_{a2}) adjusts accordingly from 30.7° to 79.2° to maintain its PT-symmetric operation. The voltage across the

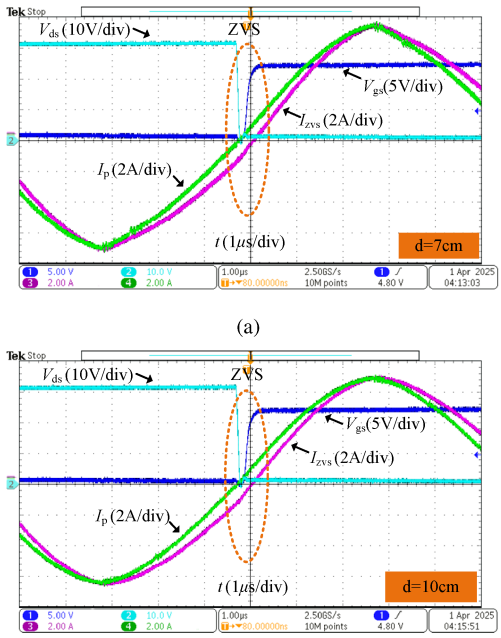

Fig. 18. ZVS operation of the inverter. (a) $d = 7$ cm. (b) $d = 10$ cm.

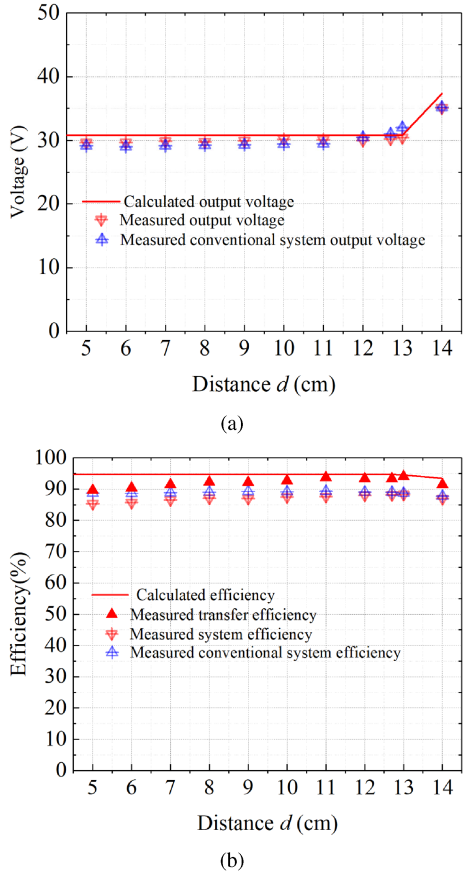

Fig. 19. Comparative experiment between the proposed method and conventional method at a load of 8 Ω with varying distance. (a) Output voltage versus distance. (b) Efficiency versus distance.

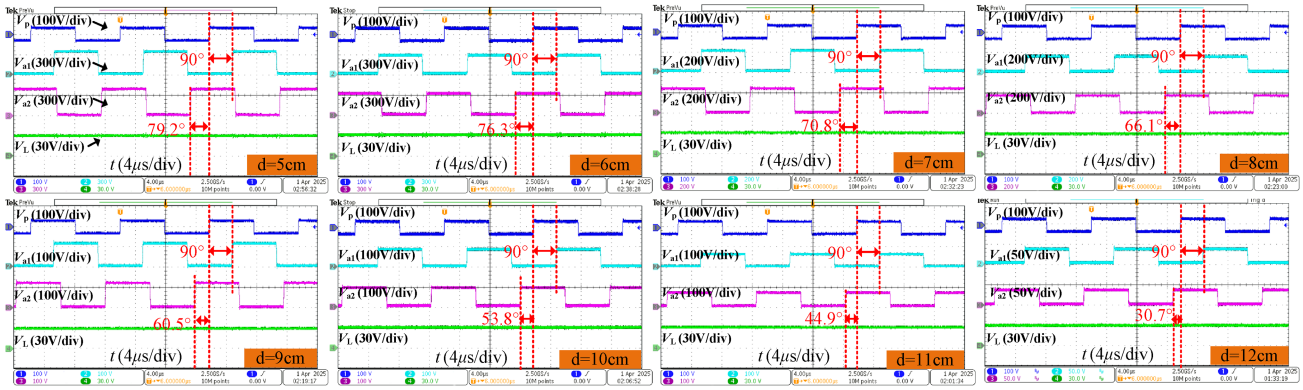

Fig. 20. The phase angle between V_{p} (output voltage of the inverter) and V_{a1} (voltage across the Tx-sides SCC) is 90°, and the phase angle between V_{p} and V_{a2} (voltage across the Rx-sides SCC) is β_1 that changes as the distance d varies.

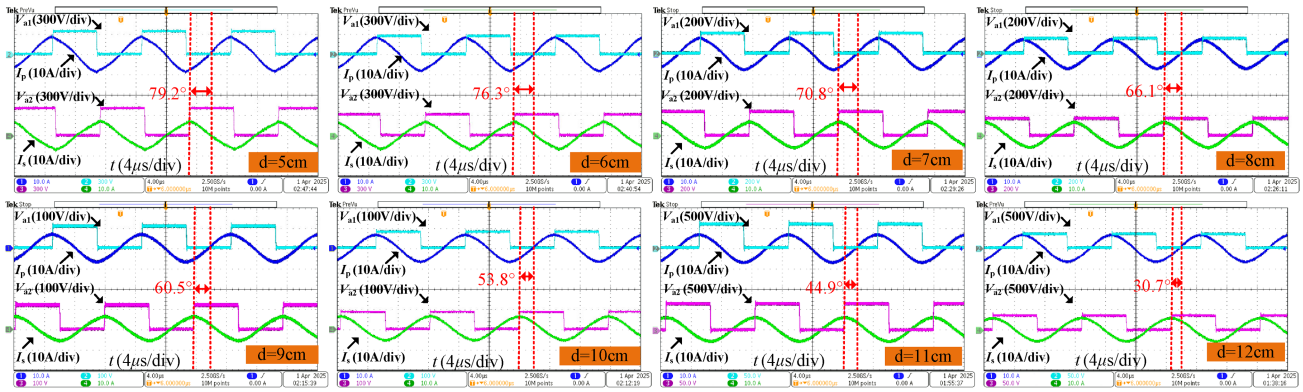

Fig. 21. Voltage (V_{a1} and V_{a2}) and current (I_{p} and I_{s}) across SSCs as the distance d varies.

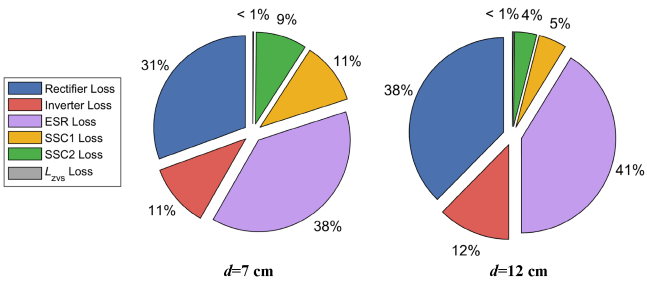

Fig. 22. Losses distribution in the system.

SCCs increases with the phase angle β_1 due to the decreasing equivalent capacitance of the SCCs.

4) Power Losses of the System: Fig. 22 presents the typical loss distribution within the system at a load of $R = 8\ \Omega$ when $d = 7$ and $d = 12$ cm. Here, $P_{L_{\mathrm{zvs}}}$, $P_{\mathrm{rectifier}}$, P_{inverter}, P_{SCC1}, P_{SCC2}, and P_{ESRs} represent the losses in the inductor L_{zvs}, rectifier, inverter, Tx-side SCC, Rx-side SCC, and the ESRs of the two resonators, respectively. It is evident that the losses in the rectifier and the ESRs of the two resonators constitute the major portion. Specifically, they reach 69% of the total losses at $d = 7$ cm and 79% at $d = 12$ cm. To enhance the efficiency further, synchronous rectification and optimized coils can be adopted.

5) Impact of Compensation Capacitor Variations on Both Sides: Fig. 23(a) and (b) illustrate the output voltage and efficiency under various compensation capacitance conditions. The normalized compensation capacitance of the Tx-side (γ_1) and Rx-side (γ_2) vary by 14.3% and 16.8%, respectively. For comparison, experiments using the conventional method were conducted under the same experimental conditions. The figures show that as the distance increases, the efficiency of the conventional method gradually declines, showing a reduction greater than 10%. Moreover, the output voltage of the conventional method fluctuates significantly, with a variation range exceeding 60%. In contrast, our method not only ensures a stable output voltage but also maintains relatively high efficiency. It is important to note that larger compensation capacitances result in higher voltage stress across the SSCs. Therefore, selecting a smaller capacitance within the allowable range can help mitigate voltage stress on the SSCs.

6) Variable Load Conditions: According to theoretical analysis, when the ESRs are negligible, the system can maintain a constant output voltage even under varying load conditions. Fig. 24 illustrates the system efficiency and output voltage with a load resistance of $R = 16\ \Omega$. It is evident that the output voltage remains nearly constant within the PT-symmetric region. Furthermore, the system efficiency remains above 91.2%, with a peak efficiency reaching 93.9%.

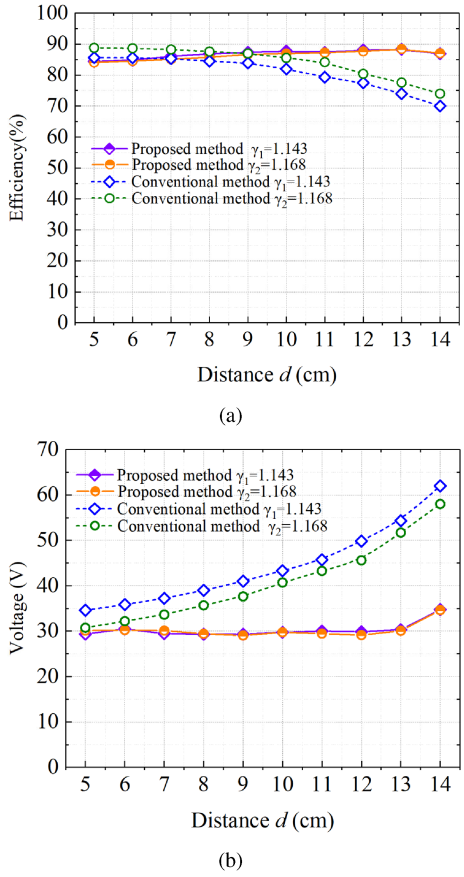

Fig. 23. Comparative experiment between the proposed method and the conventional method at a load of 8 Ω. The normalized capacitance on the Tx-side and Rx-side varies by 14.3% and 16.8%, respectively. (a) Output voltage versus distance. (b) Efficiency versus distance.

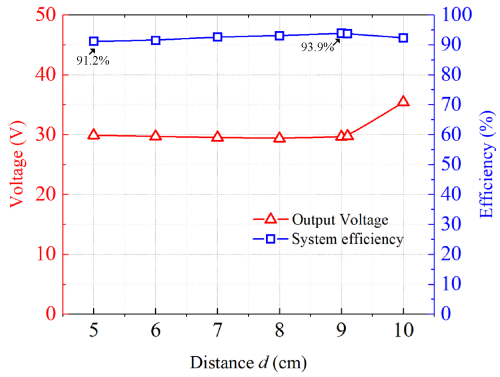

Fig. 24. Output voltage and system efficiency at a load of 16 Ω with varying distance.

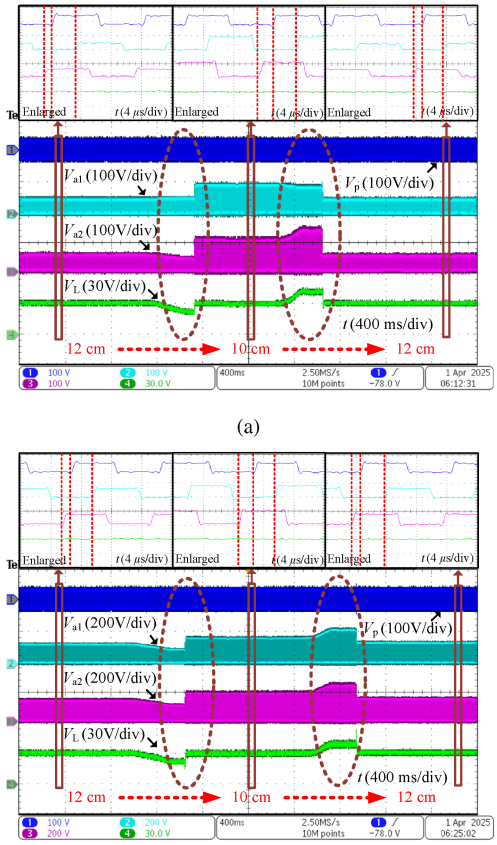

Fig. 25. Dynamic waveforms of the system when the distance changes. (a) $\gamma_1 = \gamma_2 = 1$. (b) $\gamma_1 = 1.143$, $\gamma_2 = 1.168$.

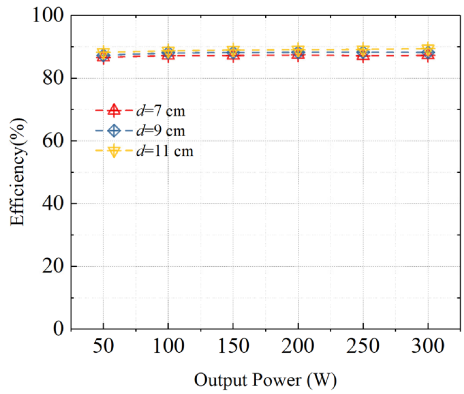

Fig. 26. System efficiency versus output power at a load of 8 Ω.

7) Time-Domain Response of the System: Fig. 25(a) and (b) show the dynamic response of the system under the conditions of $\gamma_1 = \gamma_2 = 1$ and $\gamma_1 = 1.143, \gamma_2 = 1.168$. When the distance changes from 12 cm to 10 cm and then back to 12 cm, the phase angle β_1 can adjust accordingly to maintain PT-symmetric operation. Due to the experimental constraints, the distance change was performed manually.

8) Higher-Power Operation: Fig. 26 shows the system efficiency as the output power increases. It can be seen that the system efficiency remains nearly constant. A slight improvement in efficiency at higher power levels is attributed to the reduced relative power loss. Furthermore, if necessary, higher-rated switching devices can be utilized to enable higher power transmission.

C. Comparison With Previous Related Works

1) Comparison With Previous Works on PT Symmetry: Previous studies have primarily focused on inverter topologies [2], [4], [5], compensation networks [9], [12], [13], or hybrid control

TABLE III
COMPARISON WITH EXISTING WORKS RELATED TO PT SYMMETRY

Ref.	Comp.	Inversion topology	Control scheme	Output power	System efficiency	Capacitance drift tolerance[1]	Fixed-frequency operation[2]
[2] @2024	SS	Op-amp	Self-oscillation	30 W	~87%-93.82%	No	No (70–112 kHz)
[4] @2023	SS	Class E		165 W	92.6%	No	No (160–200 kHz)
[5] @2019	SS	Half-bridge		10 W	83.7%	No	No (0.8–1 MHz)
[9] @2021	SS+series inductor	Full-bridge		155.1 W	89.4%	No	No (300–330 kHz)
[12] @2023	S-PS			26 W	89%	No	No (320–370 kHz)
[13] @2023	S-SLDC			75 W	87.5%	No	No (90–100 kHz)
[17] @2022	SS		Self-oscillation and pulse width modulation	500 W	~80%-95.6%	No	No (275–300 kHz)
This work	SS		Dual-side active tuning	100 W	85.1-93.9%	Yes ($\geq$ 14%)	Yes (85 kHz)

[1] Capacitance drift disrupts PT symmetry, leading to significant performance degradation.
[2] The operating frequency is strongly dependent on the coupling coefficient. A wider coupling range results in greater frequency variation.

TABLE IV
COMPARISON WITH RESEARCH ON DUAL-SIDE ACTIVE TUNING

Ref.	Comp.	Control units	Regulation mechanism	Control strategy	Coupling range	Control target	System efficiency	Variation tolerance		Wireless communication
								Self-inductance	Capacitance	
[30] @2023	LCC/LCC	• Dual-side SCCs	Error-driven control	Gradient descent and PI	0.165–0.321	Output power & ZVS	87.5–91.5%	Yes	–	No
[31] @2024	LCC/LCC	• Dual-side SCCs • Inverter • Active rectifier		Calculations and PI	0.3458	Output voltage & ZVS	about 87–95.16%	–	–	Yes
[32] @2025	SS	• Dual-side SCCs • Semi-active rectifier		Gradient descent and 2×PI	0.1–0.55	Output power & ZVS	86.51–95.45%	Yes	–	Yes
[33] @2025	SS	• Dual-side SCCs		2×PI	0.131–0.335	Output power & ZVS	93.1–93.8%	Yes	–	No
[34] @2025	LCC/S	• Dual-side SCCs		AS-P&O and PI	0.32–0.69	Output voltage & ZVS	about 88–92.19%	Yes	–	No
This work	SS	• Single SCC	PT-symmetric self-consistency	Calculation (Low)	0.109–0.518	PT symmetry & ZVS	85.1–93.9%	Yes	Yes	No

schemes [17]. However, the issue of parameter drift in compensation capacitance–a critical concern in practical applications due to temperature variations and manufacturing tolerances–has received limited attention. Although [9] and [13] examined the effect of capacitance drift on power transfer efficiency, they did not address its impact on output voltage regulation. In addition, a wider coupling coefficient range often results in a broader operating frequency span, posing additional challenges for filter design and compliance with frequency band regulations. Furthermore, slight resonator detuning can cause transitions between eigenfrequencies, further exacerbating frequency variation. Since most existing methods are based on self-oscillation, the aforementioned issues are commonly observed.

In contrast, our method offers a new paradigm for realizing PT symmetry through parameter tuning rather than self-oscillation. This enables fixed-frequency PT operation and exhibits high tolerance to variations in resonant parameters.

2) Comparison With Previous Works on Dual-Side Active Tuning: Table IV compares the proposed method with several recent dual-side tuning approaches that mainly target output power regulation and ZVS. Most of these approaches rely on detuned circuit models and utilize error-driven, multiloop control schemes to compensate for performance degradation caused by parameter variations. Typically, these systems incorporate multiple PI controllers [30], [31], [32], [33], [34], along with intelligent algorithms such as gradient descent [30], [32] and perturb-and-observe (P&O) methods [34], to coordinate the adjustment of switching capacitors on both the Tx and Rx sides.

In contrast, the system stabilizes the output by reconstructing the PT-symmetric condition, leveraging the system's intrinsic dynamics rather than relying on error-driven corrective control.

It does not require wireless communication [31], [32], additional sensors [30], [31], [32], [33], [34], or iterative optimization algorithms [30], [32], [34]. The control architecture is based on a single-loop scheme, which reduces system complexity and mitigates potential stability issues associated with multiloop coordination. The Rx-side controller performs basic computations using local dc voltage and current measurements, while the Tx-side controller merely generates fixed PWM signals without dynamic adjustment.

VI. Conclusion

This article proposes a simple dual-side tuning approach to realize fixed-frequency PT-symmetric operation. Leveraging the synchronous characteristics of SSCs, the method enables a single active adjustment (on the Rx side) to inherently balance gain and loss with the Tx-side compensator self-adjusting in response. PT symmetry is maintained by adaptively tuning the Rx-side compensation parameters as the coupling coefficient and load vary. Notably, changing the compensation capacitors within a certain range does not affect the system's performance. In other words, capacitors with larger tolerances can be used. Furthermore, this method easily achieves ZVS. Since the input impedance remains purely resistive, an appropriate parallel inductor can be selected to ensure ZVS operation across the entire operating range. Experimental results demonstrate that the proposed method can maintain fixed-frequency PT-symmetric operation as the coupling coefficient varies from 0.109 to 0.518 (5 to 12.7 cm). Within this range, the output voltage remains nearly constant. In addition, it has been validated that when the self-inductance changes by 10.68%, and compensation capacitors on the Tx and Rx sides change by 14.3% and 16.8%, respectively, the fixed-frequency PT-symmetric operation is almost unaffected. In summary, the contributions of this article are as follows:

1) robustness against variations in compensation capacitance, self-inductance, coupling coefficient, and load;
2) achieving PT-symmetric operation with a fixed operating frequency; and
3) ensuring ZVS operation across the entire operating range.

References

[1] S. Assawaworrarit, X. Yu, and S. Fan, "Robust wireless power transfer using a nonlinear parity–time-symmetric circuit," *Nature*, vol. 546, no. 7658, pp. 387–390, Jun. 2017.

[2] Z.-J. Liao, J.-L. Yi, Q.-W. Zhu, Z.-Y. Jin, and C.-Y. Xia, "Power and distance enhancement in parity-time symmetric magnetic coupling wireless power transfer systems," *IEEE J. Emerg. Sel. Topics Power Electron.*, vol. 13, no. 4, pp. 4191–4204, Aug. 2025.

[3] S. Assawaworrarit and S. Fan, "Robust and efficient wireless power transfer using a switch-mode implementation of a nonlinear parity–time symmetric circuit," *Nat. Electron.*, vol. 3, no. 5, pp. 273–279, Apr. 2020.

[4] L. He, X. Huang, and B. Cheng, "Robust Class E^2 wireless power transfer system based on parity–time symmetry," *IEEE Trans. Power Electron.*, vol. 38, no. 4, pp. 4279–4288, Apr. 2023.

[5] J. Zhou, B. Zhang, W. Xiao, D. Qiu, and Y. Chen, "Nonlinear parity-time-symmetric model for constant efficiency wireless power transfer: Application to a drone-in-flight wireless charging platform," *IEEE Trans. Ind. Electron.*, vol. 66, no. 5, pp. 4097–4107, May 2019.

[6] L. Wu, B. Zhang, and J. Zhou, "Efficiency improvement of the parity-time-symmetric wireless power transfer system for electric vehicle charging," *IEEE Trans. Power Electron.*, vol. 35, no. 11, pp. 12497–12508, Nov. 2020.

[7] H. Chen, D. Qiu, C. Rong, and B. Zhang, "A double-transmitting coil wireless power transfer system based on parity-time symmetry principle," *IEEE Trans. Power Electron.*, vol. 38, no. 11, pp. 13396–13404, Nov. 2023.

[8] X. Shu, B. Zhang, Z. Wei, C. Rong, and S. Sun, "Extended-distance wireless power transfer system with constant output power and transfer efficiency based on parity-time-symmetric principle," *IEEE Trans. Power Electron.*, vol. 36, no. 8, pp. 8861–8871, Aug. 2021.

[9] Z. Wei and B. Zhang, "Transmission range extension of PT-symmetry-based wireless power transfer system," *IEEE Trans. Power Electron.*, vol. 36, no. 10, pp. 11135–11147, Oct. 2021.

[10] C. Rong, B. Zhang, Z. Wei, L. Wu, and X. Shu, "A wireless power transfer system for spinal cord stimulation based on generalized parity–time symmetry condition," *IEEE Trans. Ind. Appl.*, vol. 58, no. 1, pp. 1330–1339, Jan./Feb. 2022.

[11] Y. Qu, B. Zhang, W. Gu, and X. Shu, "Wireless power transfer system with high-order compensation network based on parity-time-symmetric principle and relay coil," *IEEE Trans. Power Electron.*, vol. 38, no. 1, pp. 1314–1323, Jan. 2023.

[12] Y. Qu, B. Zhang, W. Gu, J. Li, and X. Shu, "Distance extension of S-PS wireless power transfer system based on parity-time symmetry," *IEEE Trans. Circuits Syst. II Exp. Briefs*, vol. 70, no. 8, pp. 2954–2958, Aug. 2023.

[13] Y. Gu, J. Wang, Z. Liang, and Z. Zhang, "A wireless in-flight charging range extended PT-WPT system using S/single-inductor-double-capacitor compensation network for drones," *IEEE Trans. Power Electron.*, vol. 38, no. 10, pp. 11847–11858, Oct. 2023.

[14] J. Liu, X. Qu, Y. Li, and C. Ma, "Investigation of PT-symmetric frequency and compensation for IPT coupling-independent CC/CV and efficiency in wide load range," *IEEE Trans. Power Electron.*, vol. 38, no. 11, pp. 13353–13362, Nov. 2023.

[15] C. Luo, D. Qiu, W. Gu, B. Zhang, Y. Chen, and W. Xiao, "Multiload wireless power transfer system with constant output power and efficiency," *IEEE Trans. Ind. Appl.*, vol. 58, no. 1, pp. 1101–1114, Jan./Feb. 2022.

[16] L. Wu, B. Zhang, and Y. Jiang, "Position-independent constant current or constant voltage wireless electric vehicles charging system without dual-side communication and DC–DC converter," *IEEE Trans. Ind. Electron.*, vol. 69, no. 8, pp. 7930–7939, Aug. 2022.

[17] L. Wu, B. Zhang, Y. Jiang, and J. Zhou, "A robust parity-time-symmetric WPT system with extended constant-power range for cordless kitchen appliances," *IEEE Trans. Ind. Appl.*, vol. 58, no. 1, pp. 1179–1189, Jan./Feb. 2022.

[18] Z. Hua, K. T. Chau, W. Liu, and X. Tian, "Pulse frequency modulation for parity-time-symmetric wireless power transfer system," *IEEE Trans. Magn.*, vol. 58, no. 8, Aug. 2022, Art. no. 8002005.

[19] L. Wu, B. Zhang, and Y. Jiang, "Robust parity-time-symmetric WPT system with reduced switching-frequency and improved step-down conversion ratio," *IEEE Trans. Transp. Electron.*, vol. 9, no. 2, pp. 2090–2103, Jun. 2023.

[20] J. Li, X. Liu, and K. N. Leung, "A 24-to-240w 95.6%-efficiency < 300-μs-settling-time hybrid MCR/PT wireless power transfer system," *IEEE Trans. Power Electron.*, vol. 39, no. 7, pp. 8928–8946, Jul. 2024.

[21] L. Wu, B. Zhang, and Y. Jiang, "Output-power-controllable parity-time-symmetric wireless power transfer system with soft switching for kitchen appliances," *IEEE Trans. Consum. Electron.*, vol. 70, no. 4, pp. 6630–6640, Nov. 2024, doi: 10.1109/TCE.2024.3470112.

[22] S. Sun, B. Zhang, C. Rong, X. Shu, and Z. Wei, "A multireceiver wireless power transfer system using self-oscillating source composed of zero-voltage switching full-bridge inverter," *IEEE Trans. Ind. Electron.*, vol. 69, no. 3, pp. 2885–2895, Mar. 2022.

[23] J. Wu, K. Li, J. Zeng, and S.-Y. R. Hui, "On the limitations of the coupled mode theory and parity-time symmetry for near-field wireless power transfer research," *IEEE Trans. Power Electron.*, vol. 39, no. 5, pp. 6433–6441, May 2024.

[24] Y. Endo and Y. Furukawa, "Proposal for a new resonance adjustment method in magnetically coupled resonance type wireless power transmission," in *Proc. Int. Microw. Workshop Ser. Innov. Wireless Power Transmiss., Technol., Syst. Appl.*, Kyoto, Japan, 2012, pp. 263–266.

[25] L. Shi, P. Alou, J. Á. Oliver, J. C. Rodriguez, A. Delgado, and J. A. Cobos, "A self-adaptive wireless power transfer system to cancel the reactance," *IEEE Trans. Ind. Electron.*, vol. 68, no. 12, pp. 12141–12151, Dec. 2021.

[26] D. J. Thrimawithana, U. K. Madawala, and M. Neath, "A synchronization technique for bidirectional IPT systems," *IEEE Trans. Ind. Electron.*, vol. 60, no. 1, pp. 301–309, Jan. 2013.

[27] R. Mai, Y. Liu, Y. Li, P. Yue, G. Cao, and Z. He, "An active-rectifier-based maximum efficiency tracking method using an additional measurement coil for wireless power transfer," *IEEE Trans. Power Electron.*, vol. 33, no. 1, pp. 716–728, Jan. 2018.

[28] K. Song et al., "An impedance decoupling-based tuning scheme for wireless power transfer system under dual-side capacitance drift," *IEEE Trans. Power Electron.*, vol. 36, no. 7, pp. 7526–7536, Jul. 2021.
[29] W. Li, Q. Zhang, C. Cui, and G. Wei, "A self-tuning S/S compensation WPT system without parameter recognition," *IEEE Trans. Ind. Electron.*, vol. 69, no. 7, pp. 6741–6750, Jul. 2022.
[30] Z. Luo, Y. Zhao, M. Xiong, X. Wei, and H. Dai, "A self-tuning LCC/LCC system based on switch-controlled capacitors for constant-power wireless electric vehicle charging," *IEEE Trans. Ind. Electron.*, vol. 70, no. 1, pp. 709–720, Jan. 2023.
[31] G. Zhu, J. Dong, T. B. Soeiro, H. Vahedi, and P. Bauer, "Dual-side capacitor tuning and cooperative control for efficiency-optimized wide output voltages in wireless EV charging," *IEEE Trans. Ind. Electron.*, vol. 72, no. 3, pp. 2507–2518, Mar. 2025.
[32] B. Zou, Z. Huang, I.-W. Iam, and C.-S. Lam, "Tuning control against coupler parameter variations due to misalignment in an optimal-efficiency-tracking and constant-power-output IPT system," *IEEE Trans. Power Electron.*, vol. 40, no. 5, pp. 7500–7511, May 2025.
[33] R. Matsumoto, T. Fujita, and H. Fujimoto, "Reactance decompensation using PWM-controlled switched capacitors for maintaining constant power and efficiency in S/S WPT systems," *IEEE J. Emerg. Sel. Top. Power Electron.*, early access, May 20, 2025, doi: 10.1109/JESTPE.2025.3571712.
[34] J. Xie, Y. Chen, S. Qu, C. Luo, and J. Guo, "Dual-side adaptive tuning cooperative control for tracking zero phase angle and maximum output voltage in dynamic LCC-S WPT system," *IEEE J. Emerg. Sel. Top. Power Electron.*, early access, Apr. 30, 2025, doi: 10.1109/JESTPE.2025.3565744.

Ruozhong Gao was born in Shanxi, China. He received the B.S. and M.Sc. degrees in electrical engineering from the Taiyuan University of Technology, Taiyuan, China, in 2013 and 2017, respectively. He is currently working toward the Ph.D. degree in control theory and control engineering with Chongqing University, Chongqing, China.

His current research interests include wireless power transfer applications and power electronics.

Xin Dai (Member, IEEE) received the B.S. degree in industrial automation from Yuzhou University, Chongqing, China, in 2000, and the Ph.D. degree in control theory and control engineering from the School of Automation, Chongqing University, Chongqing, in 2006.

In 2012, he was a Visiting Scholar with the University of Auckland, Auckland, New Zealand. He is currently a Professor with the School of Automation, Chongqing University. His research interests include inductive power transfer technology and nonlinear dynamic behavior analysis of power electronics.

Shijun Zhao (Member, IEEE) was born in Sichuan, China. He received the B.Eng. degree in automation from the Faculty of Information Engineering and Automation, Kunming University of Science and Technology, Yunnan, China, in 2017. He is currently working toward the Ph.D. degree in control theory and control engineering with Chongqing University, Chongqing, China.

His current research interests include modeling, system identification, and control methods of wireless power transfer and power electronics.

Pengqi Deng received the B.E. degree in automation and the Ph.D. degree in control theory and control engineering from the College of Automation, Chongqing University, Chongqing, China, in 2015 and 2024, respectively.

Since 2024, he has been with the College of Optoelectronics Engineering, Chongqing University of Posts and Telecommunications, Chongqing, where he is currently a Postdoctoral Researcher. His research interests include nonlinear modeling and analysis, electromagnetic interference suppression, and wireless power transfer.

Jinde Wu received the B.S. degree from the College of Information Engineering, Taiyuan University of Technology, Taiyuan, China, in 2015, and the Ph.D. degree in control theory and control engineering from the School of Automation, Chongqing University, Chongqing, China, in 2021.

He is currently with the College of Electrical and Power Engineering, Taiyuan University of Technology. His main research interests cover wireless power transfer, computer vision, and intelligent sensor and detection technology.

Yanling Li received the B.Sc. degree from Yuzhou University in 2000, the M.Sc. degree from the University of Electronic Science and Technology, Chengdu, China, in 2007, and the Ph.D. degree from Chongqing University, Chongqing, China, in 2017.

She is currently an Associate Professor with the School of Electrical Engineering and Electronic Information, Xihua University, Chengdu, China. Her research interests include wireless power transfer technology, control theory, and applications.